


# Aligning High-Aspect-Ratio Particles in User-Specified Orientations with Ultrasound-Directed Self-Assembly

M. Prisbrey and B. Raeymaekers\*

*Department of Mechanical Engineering, University of Utah, Salt Lake City, Utah 84112, USA*

 (Received 2 April 2019; revised manuscript received 3 June 2019; published 9 July 2019)

We use ultrasound directed self-assembly (DSA) to create two-dimensional patterns of high-aspect-ratio particles with user-specified orientation. We theoretically derive a method to determine the operating parameters of any arrangement of ultrasound transducers required to align high-aspect-ratio particles in any user-specified orientation. The method finds the ultrasound wave field that maximizes the curvature of the acoustic radiation potential orthogonal to the user-specified particle orientation and in user-specified locations. We simulate the theoretical solution resulting from this method and experimentally validate it using carbon microfibers in water and quantify the position and orientation error. This method enables controlling the location and orientation of high-aspect-ratio particles, including simultaneously orienting multiple high-aspect-ratio particles in different directions. This work finds application in the biomedical field and in using ultrasound DSA as a processing or manufacturing method for engineered materials.

DOI: [10.1103/PhysRevApplied.12.014014](https://doi.org/10.1103/PhysRevApplied.12.014014)

## I. INTRODUCTION

Directed self-assembly (DSA) is the process by which discrete components organize into patterns due to interactions between themselves and their environment, driven by internal or external forces [1]. DSA techniques enable organizing particles into user-specified patterns and play an important role in a myriad of applications, including biology [2], biomedical devices [3], and manufacturing engineered materials [4–8]. The literature categorizes DSA techniques as template [9,10], template free [11], and external field-directed techniques [12–20]. External field-directed self-assembly employs a set of transducers to generate an electric [12], magnetic [13], or ultrasound field [21,22]. The operating parameters and arrangement of the transducers determine the resulting external field, which directly relates to the locations where particles assemble. Magnetic and electric external field-directed techniques require ferromagnetic and electrically conductive particles, respectively, and typically demand ultrahigh field strengths to move particles into their desired locations [12,13]. In contrast, ultrasound DSA relies on the convergence of the radiation force associated with an ultrasound wave field, which creates acoustic “traps” that capture particles and allow controlling their location independent of their material properties [23] and shape [24]. Furthermore, low attenuation of ultrasound waves in low-viscosity (bulk and shear) fluids [25] such as water [17,26], air [27–29], and photopolymer resin [8],

facilitates dimensional scalability over macroscale areas and volumes. Previous work by our group focused on using ultrasound DSA as a materials manufacturing technique, for instance, by integrating it with stereolithography to three-dimensional (3D) print macroscale-engineered materials with a user-specified microstructure consisting of microparticles dispersed in photopolymer [8].

Using ultrasound DSA in engineering applications requires knowing the relationship between the ultrasound transducer operating parameters (amplitude and phase), the corresponding ultrasound wave field, and the resulting pattern of particles. This relationship reduces to solving either a “forward” or “inverse” ultrasound DSA problem. The former determines the pattern of particles resulting from user-specified ultrasound transducer operating parameters [30–33], whereas the latter resolves the ultrasound transducer operating parameters necessary to assemble a user-specified pattern of particles.

Several researchers solve the inverse ultrasound DSA problem by minimizing the acoustic radiation potential or acoustic pressure to generate acoustic traps at user-specified locations, which enables manipulating a single particle along a user-specified path [17] and forming multidimensional user-specified patterns of particles [16,34–38]. However, these methods do not consider the orientation of the acoustic traps, which limits them to using spherical particles. Several researchers solve the forward ultrasound DSA problem to manipulate the orientation of high aspect ratio particles by modulating the amplitude of two superimposed orthogonal ultrasound wave fields [39] or by selectively energizing a subset of eight

\*bart.raeymaekers@utah.edu

ultrasound transducers arranged as an octagon [40] to alter the orientation of localized minima in the ultrasound radiation potential field. In one study, Marzo *et al.* [18] solve the inverse problem by maximizing the Laplacian of the acoustic radiation potential with empirically derived weight functions, thus implicitly altering the orientation of a single acoustic trap by damping the radiation force in specific directions. Using this method, they manipulate a single high aspect ratio particle of 0.6–3.1 mm in air. Nevertheless, no theoretical understanding and experimental demonstration of using ultrasound DSA to create user-specified patterns of high-aspect-ratio particles with explicitly defined user-specified orientations exists. However, this knowledge is paramount in the context of using ultrasound DSA to manufacture engineered materials in which alignment of short fibers in user-specified patterns embedded in a polymer resin could enable manufacturing materials with exotic functions and properties in combination with providing mechanical strength.

Hence, the objective of this research is to demonstrate a solution methodology to the inverse ultrasound DSA problem to create two-dimensional (2D) user-specified patterns of high-aspect-ratio particles with explicitly defined user-specified orientation for any arrangement and number of ultrasound transducers. We illustrate the functionality of this methodology by computing the operating parameters (amplitude and phase) of 16 ultrasound transducers arranged as a hexadecagon, which is required to create a user-specified pattern of high-aspect-ratio particles with a user-specified location and orientation. We experimentally align carbon microfibers in several user-specified orientations and locations, and validate the methodology by quantifying the deviation between user-specified high-aspect-ratio particle location and orientation and the experimental results.

## II. METHODS

We create patterns of high-aspect-ratio particles with explicit user-specified locations and orientations following three steps. First, we compute the ultrasound wave field in an arbitrarily shaped reservoir lined with ultrasound transducers using the boundary element method and based on Green's third identity [41], which relates the ultrasound wave field within a simply closed domain to the boundary conditions applied along the perimeter of that domain as a function of the ultrasound transducer operating parameters. Second, we represent a high-aspect-ratio particle (e.g., a fiber) by means of a rigid bead chain of spherical particles, and we calculate the acoustic radiation force acting on the bead chain using Gor'kov's radiation force theory [23] to determine the pattern of high-aspect-ratio particles resulting from the ultrasound wave field. Third, we determine the ultrasound transducer operating parameters required

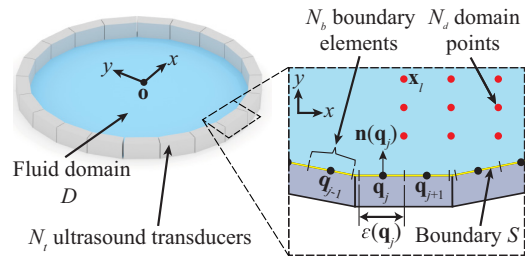


FIG. 1. Polygon-shaped reservoir lined with  $N_t$  ultrasound transducers. The inset illustrates the 2D discretization of the fluid domain  $D$  (blue) into  $N_d$  domain points (red dots) and the boundary  $S$  (yellow line) into  $N_b$  boundary elements (black dots).

to assemble a user-specified pattern of high-aspect-ratio particles with user-specified locations and orientations by solving an optimization problem in which we maximize the curvature of the acoustic radiation potential in the direction perpendicular to the user-specified orientation of the high-aspect-ratio particle by tuning the operating parameters of the ultrasound transducers (amplitude and phase).

Figure 1 shows an arbitrary polygon-shaped reservoir that contains a fluid medium of sound speed  $c_0$  and density  $\rho_0$ , and that is lined with  $N_t$  ultrasound transducers with acoustic impedance  $Z_t$ . The inset image displays the fluid domain  $D$  (blue) discretized into  $N_d$  domain points (red dots) and the boundary  $S$  (yellow line) into  $N_b \geq N_t$  boundary elements (black dots). Vectors  $\mathbf{q}_j$  and  $\mathbf{x}_l$  point to the center of each boundary element  $j$  and domain point  $l$ , respectively, from the origin of a Cartesian coordinate system  $\mathbf{o}$ , located in the center of the reservoir. Each boundary element  $\mathbf{q}_j$  is  $\varepsilon(\mathbf{q}_j)$  wide, and follows the complex harmonic velocity  $v(\mathbf{q}_j)$  (amplitude and phase) of the ultrasound transducer surface, acting as a piston source in its normal direction  $\mathbf{n}(\mathbf{q}_j)$ .

We use the boundary element method to compute the ultrasound wave field of frequency  $\omega_0$  in terms of the time-independent, complex scalar velocity potential  $\varphi$  at each domain point  $\mathbf{x}_l$  in  $D$ . We assume that at each domain point, the Helmholtz equation ( $\nabla^2 \varphi + k_0^2 \varphi = 0$ ) is satisfied, and that the impedance boundary condition ( $\partial \varphi / \partial \mathbf{n} + ik_0 Z \varphi = v$ ) is met. Here,  $i = \sqrt{-1}$ ,  $k_0 = 2\pi/\lambda_0$  is the wave number,  $\lambda_0$  is the wavelength of the ultrasound wave field in the fluid,  $Z = \rho_0 c_0 / Z_t$  is the impedance ratio between the fluid and ultrasound transducer surface, which accounts for reflection and absorption of the ultrasound wave as it interacts with the ultrasound transducers, and  $v$  is the complex harmonic velocity of the ultrasound transducer surface. We compute the ultrasound wave field  $\varphi$  in all domain points as a function of the ultrasound transducer operating parameters  $\mathbf{v}$  as [41]

$$\varphi = \mathbf{P}\mathbf{W}\mathbf{v}. \quad (1)$$

Each element in the vector  $\mathbf{v}$  contains the operating parameters (amplitude and phase) for each of the  $N_t$  ultrasound transducers. The matrix  $\mathbf{W}$  maps the boundary elements to the corresponding ultrasound transducer, that is, if the  $j$ th boundary element is contained within the  $n$ th ultrasound transducer,  $w_{jn} = 1$ , otherwise  $w_{jn} = 0$ . Each term  $p_{lj}$  in  $\mathbf{P}$  represents the ultrasound wave field generated at each domain point  $\mathbf{x}_l$  by each boundary element  $\mathbf{q}_j$ , which we calculate in matrix form as [16]

$$\mathbf{P} = \mathbf{B}_d - \mathbf{A}_d \left( \frac{1}{2} \mathbf{I} + \mathbf{A}_b \right)^{-1} \mathbf{B}_b. \quad (2)$$

$\mathbf{I}$  is the identity matrix. We determine each term  $a_{lj}$  and  $b_{lj}$  in  $\mathbf{A}_b$  and  $\mathbf{B}_b$  as

$$a_{lj} = \left[ ik_0 ZG(\mathbf{q}_j, \mathbf{x}_l) + \frac{\partial G(\mathbf{q}_j, \mathbf{x}_l)}{\partial \mathbf{n}(\mathbf{q}_j)} \right] \times \varepsilon(\mathbf{q}_j) \delta(\mathbf{q}_j, \mathbf{x}_l) \quad (3)$$

and

$$b_{lj} = G(\mathbf{q}_j, \mathbf{x}_l) \varepsilon(\mathbf{q}_j) \delta(\mathbf{q}_j, \mathbf{x}_l). \quad (4)$$

Here,  $\delta(\mathbf{q}_j, \mathbf{x}_l) = 0$  if  $\mathbf{q}_j = \mathbf{x}_l$ , otherwise  $\delta(\mathbf{q}_j, \mathbf{x}_l) = 1$ , and  $G(\mathbf{q}_j, \mathbf{x}_l)$  is Green's function, which represents the free-field ultrasound wave at point  $\mathbf{x}_l$  emitted from a point source at  $\mathbf{q}_j$ , computed as [41]

$$G(\mathbf{q}_j, \mathbf{x}_l) = -\frac{i}{4} H_0(k_0 |\mathbf{q}_j - \mathbf{x}_l|). \quad (5)$$

$H_0$  is the zeroth-order Hankel function of the first kind and  $|\mathbf{q}_j - \mathbf{x}_l|$  is the Euclidean distance between the point source  $\mathbf{q}_j$  and domain point  $\mathbf{x}_l$ . We determine  $\mathbf{A}_d$  and  $\mathbf{B}_d$  analogously to  $\mathbf{A}_b$  and  $\mathbf{B}_b$ , but the subscripts  $d$  and  $b$  in Eq. (2) indicate if the test point  $\mathbf{x}_l$  lies in the fluid domain  $D$ , or on the boundary  $S$ , respectively.

We use Gor'kov's acoustic radiation force theory to relate the ultrasound wave field to the location and orientation of the acoustic traps where particles will accumulate [23]. The acoustic trap locations  $\mathbf{x}_s$  are defined as the locations where the acoustic radiation potential  $U_l$  is locally minimum, and the acoustic radiation force  $\mathbf{f}_l = -\nabla U_l$  is zero and points toward  $\mathbf{x}_s$  in the surrounding region.  $U_l = \mathbf{v}^H \mathbf{Q}_l \mathbf{v}$ , with  $\mathbf{v}^H$  the complex conjugate transpose of the vector that contains the ultrasound transducer operating parameters  $\mathbf{v}$ , and we calculate the Hermitian matrix  $\mathbf{Q}_l$  as [16]

$$\mathbf{Q}_l = 2\pi r_p^3 \rho_0 \mathbf{W}^H \left\{ \frac{1}{3} k_0^2 \left[ 1 - \left( \frac{\rho_0 c_0}{\rho_p c_p} \right)^2 \right] [\mathbf{p}_l \mathbf{p}_l^H] - \left[ \frac{\rho_p - \rho_0}{2\rho_p + \rho_0} \right] [(\nabla \mathbf{p}_l)(\nabla \mathbf{p}_l)^H] \right\} \mathbf{W}, \quad (6)$$

with  $r_p \ll \lambda_0$  the radius of a spherical particle with sound propagation speed  $c_p$  and density  $\rho_p$ .  $\mathbf{p}_l^H$  is the  $l$ th row of

matrix  $\mathbf{P}$  [see Eq. (2)]. We assume the primary acoustic radiation forces dominate over secondary scattering forces resulting from other nearby particles and thus, do not consider these secondary scattering forces in our model.

We determine the orientation  $\theta_s$  of each acoustic trap  $\mathbf{x}_s$  and thus, the orientation of a high-aspect-ratio particle in that location, composed from a rigid bead chain of spherical particles, as the direction perpendicular to the direction of maximum curvature of the acoustic radiation potential. We model each spherical bead of the bead chain with a radius  $r_p$  equal to the radius of the microfiber we use in the experiments, and the center points of the spherical beads are  $2r_p$  apart. Hence, each bead chain consists of  $l_f/2r_p = 72$  beads, where  $l_f$  is the length of the microfiber. The direction of maximum curvature at any domain point  $\mathbf{x}_l$  is the eigenvector associated with the largest eigenvalue of the Hessian of the acoustic radiation potential at that location. We compute the curvature of the acoustic radiation potential perpendicular to any orientation  $\theta_l$  at a location  $\mathbf{x}_l$  in  $D$  as

$$\kappa_l(\mathbf{x}_l, \theta_l) = \mathbf{v}^H \hat{\mathbf{Q}}_l \mathbf{v}, \quad (7)$$

$$\hat{\mathbf{Q}}_l = \sin^2(\theta_l) \frac{\partial^2 \mathbf{Q}_l}{\partial x^2} - 2 \sin(\theta_l) \cos(\theta_l) \frac{\partial^2 \mathbf{Q}_l}{\partial x \partial y} + \cos^2(\theta_l) \frac{\partial^2 \mathbf{Q}_l}{\partial y^2}. \quad (8)$$

Hence, to self-assemble high-aspect-ratio particles in user-specified locations  $X_{\text{des}}$  with user-specified orientations  $\theta_{\text{des}}$ , the curvature  $\kappa_l$  must be locally maximum in the direction perpendicular to  $\theta_{\text{des}}$  at every point  $\mathbf{x}_l \in X_{\text{des}}$ . Here,  $X_{\text{des}}$  and  $\theta_{\text{des}}$  are lists of user-specified high-aspect-ratio particle locations and their corresponding user-specified orientations. We model a high-aspect-ratio particle as a rigid bead chain of spherical particles because it allows formulating the objective function to be maximized directly via eigendecomposition. However, to obtain a single objective function and optimize over all points  $\mathbf{x}_l \in X_{\text{des}}$ , we must relax the requirement of local maximality, which may result in a wave field that imparts a nonzero force and/or torque on a high-aspect-ratio particle, causing deviations between the resulting and user-specified patterns. We relax the requirement of local maximality to obtain a single objective function by maximizing the sum of  $\kappa_l$  for all points  $\mathbf{x}_l \in X_{\text{des}}$  and  $\theta_{\text{des}} \in \mathbb{R}$ , which we write as

$$\kappa_\Sigma = \mathbf{v}^H \hat{\mathbf{Q}}_\Sigma \mathbf{v}, \quad (9)$$

where  $\hat{\mathbf{Q}}_\Sigma$  is the summation of the matrices  $\hat{\mathbf{Q}}_l$  for all  $\mathbf{x}_l \in X_{\text{des}}$  and  $\theta_{\text{des}}$ . Similar to the optimization problem solved by Greenhall *et al.* [16], we constrain the amplitude of the ultrasound transducers to reflect their finite input power  $|\mathbf{v}| = \alpha$ , where  $\alpha$  is a real scalar value that represents the maximum harmonic velocity of the ultrasound transducer

surface. Finally, we formulate the constrained quadratic optimization problem as

$$\max \kappa_{\Sigma}, \text{ subject to } |\mathbf{v}| = \alpha. \quad (10)$$

From Eq. (10), we compute the ultrasound transducer operating parameters (amplitude and phase)  $\mathbf{v}^*$  required to assemble high-aspect-ratio particles in user-specified locations with user-specified orientations by calculating the eigenvector associated with the largest eigenvalue of the matrix  $\hat{\mathbf{Q}}_{\Sigma}$ . Because this optimization method solves for the optimal conditions to directly maximize the objective function, in contrast to an iterative search algorithm technique, the solution is not sensitive to a set of initial conditions nor is there a requirement to specify any.

The process of creating a user-specified pattern of high-aspect-ratio particles is as follows. We first define a user-specified orientation between  $0^\circ$  and  $90^\circ$  at the center of the reservoir. We then solve Eq. (10) to determine the ultrasound transducer operating parameters  $\mathbf{v}^*$  required to orient high-aspect-ratio particles along the user-specified orientation. Next, we validate the theoretical model by applying the ultrasound transducer operating parameters  $\mathbf{v}^*$  to an experimental setup and measuring the orientation of the experimentally obtained pattern of high-aspect-ratio particles compared to the user-specified orientation.

Figure 2 shows a schematic of the experimental setup. It consists of a hexadecagon-shaped reservoir that contains water with dispersed carbon microfibers (length  $100 \mu\text{m}$ , diameter  $7 \mu\text{m}$ ), and is lined with 16 ultrasound transducers with a center frequency of 1 MHz (piezo material SM111, manufactured by STEMINC, Doral, FL, USA). It is possible to choose ultrasound transducers that operate at different frequencies. To mitigate the effect of attractive interparticle forces between the carbon microfibers, we use sodium dodecylbenzenesulfonate (NaDDBS) as a surfactant in combination with sonication of the fluid-particle mixture prior to each experiment. The distance between any two parallel ultrasound transducers is  $4.2 \text{ cm} = 28\lambda_0$ , where  $\lambda_0 = 1.5 \text{ mm}$ , to ensure that the user-specified patterns are assembled in the far field. We use a field programmable gate array (FPGA) to drive each ultrasound

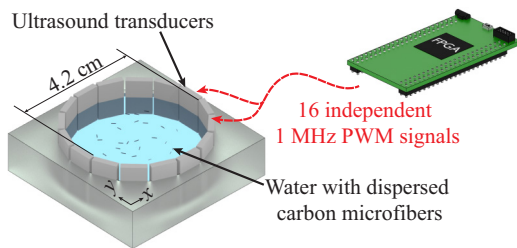


FIG. 2. Schematic of the experimental setup with 16 ultrasound transducers arranged in a hexadecagon and driven by a 1-MHz pulse width modulated signal using an FPGA.

transducer using independently controlled pulse width modulated (PWM) signals with a frequency of 1 MHz and an amplitude of 5 Vpp (peak-to-peak voltage). Controlling the PWM duty cycle and signal delay allows independently adjusting the amplitude and phase, respectively, of each ultrasound transducer. Additionally, we amplify each individual signal to a maximum of 36 Vpp via MOSFET amplifier circuits.

Figure 3 shows a schematic of a pattern of aligned microfibers (black) clustering in the acoustic traps, with a line of red dots indicating the user-specified orientation and location. We first determine the orientation of the cluster of microfibers by projecting a line from each red dot orthogonal to the user-specified orientation and computing the average location of the microfiber pattern along that projection line, which we indicate with a green dot. Hence, the green dots mark the “average” pattern of microfibers. The large inset image in Fig. 3 shows a top view of the pattern of microfibers (black) with the user-specified orientation (red dots) and the “average” location of the pattern of microfibers (green dots) superimposed. The small inset image in Fig. 3 shows a magnified view of the pattern of microfibers and the parameters that define their position  $d_i$  and orientation  $\theta_j$ . We compute the position error  $E_{\text{pos}}$  between the microfiber pattern (green dots)

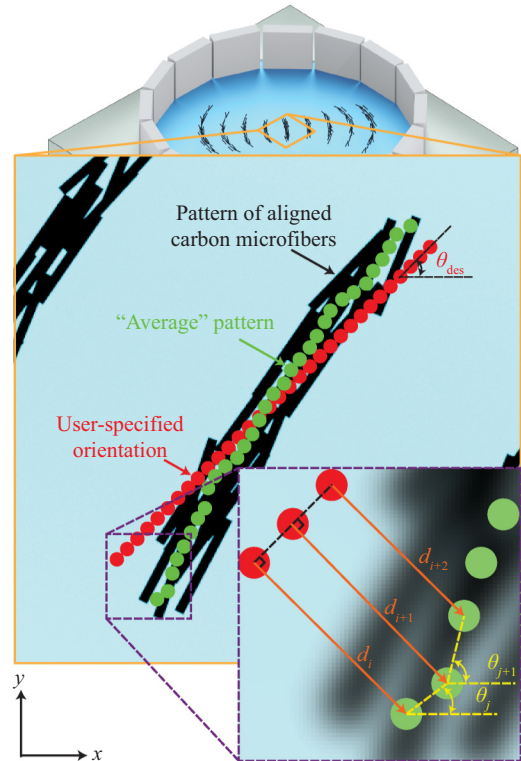


FIG. 3. Schematic of a typical pattern of aligned carbon microfibers with the large inset showing the user-specified (red dots) and actual “average” pattern (green dots). The small inset shows a magnified view indicating the parameters used to compute the pattern and orientation errors.

and user-specified pattern (red dots) as

$$E_{\text{pos}} = \frac{100}{n\lambda_0} \sum_{i=1}^n |d_i|, \quad (11)$$

which is the average distance between  $n$  corresponding red and green dots, respectively, normalized by the wavelength ( $\lambda_0 = 1.5$  mm). We also compute the orientation error  $\theta_{\text{diff}}$  between the microfiber and user-specified patterns as

$$\theta_{\text{diff}} = \frac{100}{\pi/2} \left( \theta_{\text{des}} - \frac{1}{(n-1)} \sum_{j=1}^{n-1} \theta_j \right), \quad (12)$$

which is the difference between the user-specified orientation  $\theta_{\text{des}}$  and the average of the angles between the corresponding red and green dots normalized by  $\pi/2$  radians. Using a convergence study of  $E_{\text{pos}}$  and  $\theta_{\text{diff}}$  as a function of  $n$ , we determine that the user-specified orientation must consist of at least 100 dots to accurately represent the error.

### III. RESULTS AND DISCUSSION

We assemble user-specified patterns of carbon microfibers with user-specified orientations in a water reservoir

(Fig. 2) and demonstrate independent control of the location and orientation of single (Fig. 4) and multiple (Fig. 5) clusters of carbon microfibers. Figures 4(a) and 5(a) show simulated and experimental results, respectively, with the user-specified orientation superimposed in red. Additionally, Figs. 4(b) and 5(b) show the position and orientation error as a function of user-specified orientation.

Figure 4(a) shows clusters of aligned fibers oriented at user-specified angles of  $15^\circ$ ,  $45^\circ$ ,  $55^\circ$ , and  $75^\circ$ , respectively. The top row shows the simulated acoustic radiation potential (green), designed to display local minima oriented along the user-specified angles by solving Eq. (10), with the simulated clusters of fibers aligning along those local minima. The simulated fibers (black lines) represent the orientation of minimum curvature of the acoustic radiation potential at the stable fixed positions  $\mathbf{x}_s$  (see Sec. II) within the solution domain. The bottom row shows the corresponding experimental results. We observe good qualitative agreement between the simulated microfiber orientation and the user-specified orientation, and between the simulated and experimental results. It is important to point out that most of the user-specified orientations are not parallel to any of the ultrasound transducer surfaces, because those orientations, which we indicate with vertical dashed black lines in Fig. 4(b), are straightforward to achieve with a single one-dimensional standing wave [8].

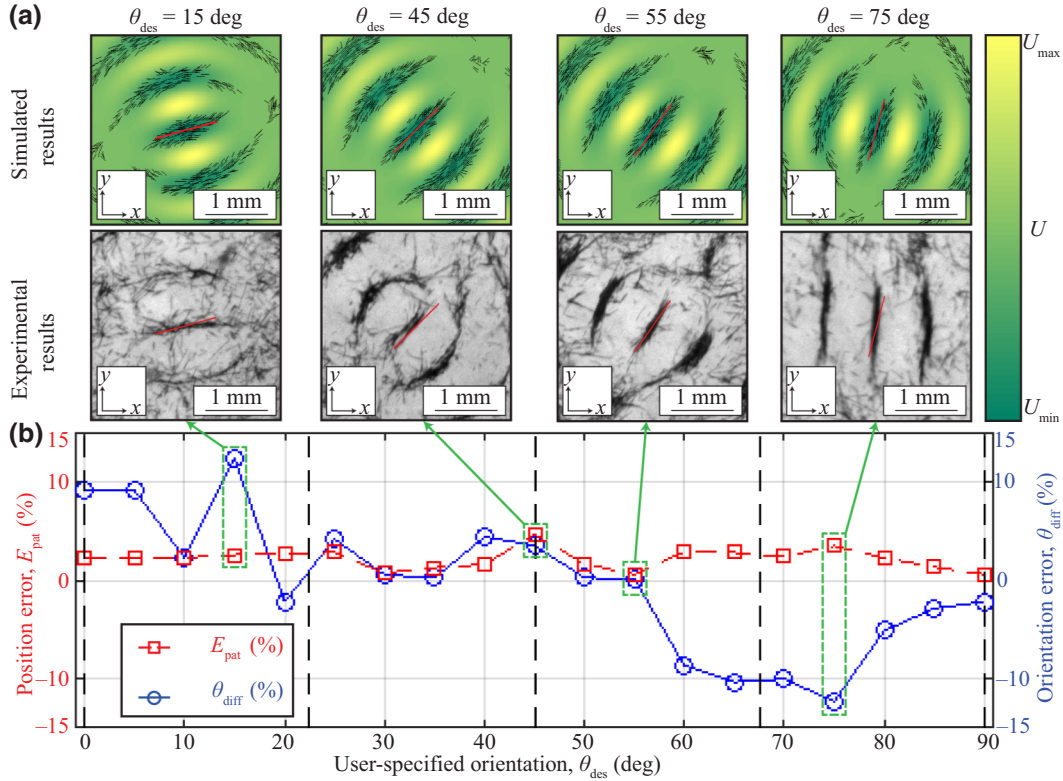


FIG. 4. (a) Simulated and experimental results for  $\theta_{\text{des}} = 15^\circ$ ,  $45^\circ$ ,  $55^\circ$ , and  $75^\circ$  showing the user-specified pattern (red line) and (b) position (red) and orientation (blue) errors as a function of user-specified orientation  $\theta_{\text{des}}$ .

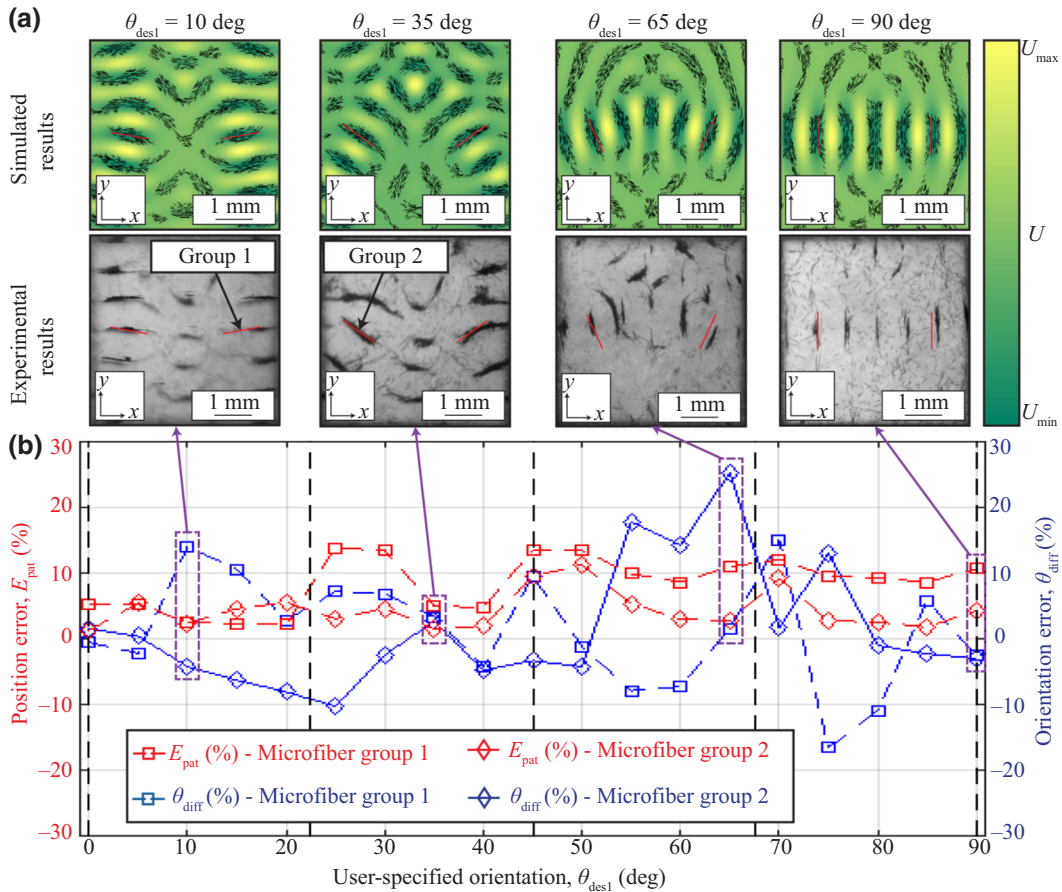


FIG. 5. (a) Simulated and experimental results for  $\theta_{\text{des}1} = 10^\circ, 35^\circ, 65^\circ, \text{ and } 90^\circ$  with the user-specified pattern (red line) and (b) position and orientation errors as a function of user-specified orientation  $\theta_{\text{des}1}$ .

The position and orientation error are independent of each other, for example,  $\theta_{\text{des}} = 55^\circ$  results in both position and orientation errors of less than 3%, whereas, for example,  $\theta_{\text{des}} = 45^\circ$  yields an orientation error of approximately 3%, but a position error of larger than 5% because the experimental pattern is offset from the user-specified orientation [see Fig. 4(a)]. Conversely,  $\theta_{\text{des}} = 15^\circ$  results in a position error of less than 3%, but an orientation error of more than 10%. Finally, for example,  $\theta_{\text{des}} = 75^\circ$  shows a position error of approximately 5% and an orientation error of more than 10%. Figure 4(b) displays the experimental position (red) and orientation (blue) errors as a function of the user-specified orientation in  $5^\circ$  increments. We observe a maximum position error of 4.6% for  $\theta_{\text{des}} = 45^\circ$  and a maximum orientation error of 12.3% for  $\theta_{\text{des}} = 15^\circ$ , demonstrating the ability to accurately assemble patterns of microfibers with user-specified orientation. Furthermore, these results show that a hexadecagonal arrangement of 16 ultrasound transducers is sufficient to maximize the curvature of the acoustic radiation potential perpendicular to any user-specified orientation. The pattern and orientation errors are due to manufacturing tolerances of the

reservoir and the transducers, alignment of the transducers, imperfections of the transducer materials and dynamics, and limitations of the hardware to generate PWM signals.

We also show user-specified patterns consisting of two groups of carbon microfibers with different user-specified orientations. For the experiments, we specify the centers of group 1 and group 2 at distances of  $\lambda_0$  and  $-\lambda_0$ , respectively, from the center of the reservoir in the  $x$  direction. We simultaneously vary the user-specified orientation of groups 1 and 2, that is,  $\theta_{\text{des}1}$  and  $\theta_{\text{des}2}$ , between  $0^\circ$  and  $90^\circ$  in  $5^\circ$  increments, with  $\theta_{\text{des}1} = -\theta_{\text{des}2}$ . Figure 5(a) shows the aligned microfibers oriented at user-specified angles of  $\theta_{\text{des}1} = 10^\circ, 35^\circ, 65^\circ, \text{ and } 90^\circ$ , respectively. The top row shows the simulated acoustic radiation potential (green) designed to display local minima oriented along the user-specified angles [solving Eq. (10)], with the simulated groups of microfibers aligning along those local minima. The bottom row shows the corresponding experimental results. Similar to the experiments with a single group of aligned microfibers shown in Fig. 4, we observe that the position and orientation errors are independent of each other. We also observe that the position and orientation

errors are different for both groups of aligned microfibers when compared to their respective user-specified orientation. For instance, for  $\theta_{\text{des}1} = 10^\circ$ , we observe a larger orientation error for group 1 than for group 2.

Extraneous groups of microfibers that are not part of the user-specified pattern exist as a result of acoustic traps existing at locations that are not in the user-specified orientation, which is an inevitable result of the standing ultrasound wave interference pattern required to create acoustic traps in the user-specified positions and orientations. Acoustic screening introduced by the extraneous groups of microfibers may cause deviations between theory and experiment. In addition, similar to assembling a single group of microfibers, error is introduced into the system by manufacturing tolerances, material imperfections, and by limitations of the electronic hardware to drive the ultrasound transducers. For instance, the FPGA that generates the PWM signals to drive the ultrasound transducers has a phase resolution of  $\pi/16$  radians and an amplitude resolution of  $V_{\text{pp}}/16$  between 0 and  $36 V_{\text{pp}}$ .

Figure 5(b) displays the experimental position (red) and orientation (blue) errors as a function of the user-specified orientation  $\theta_{\text{des}1}$  in  $5^\circ$  increments, with square markers for microfiber group 1 and round markers for microfiber group 2. The vertical black dashed lines represent orientations that are parallel to ultrasound transducer surfaces. We observe a maximum position error of 13.8% for  $\theta_{\text{des}1} = 25^\circ$  and a maximum orientation error of 25.2% for  $\theta_{\text{des}1} = 65^\circ$ , demonstrating good quantitative agreement between the user-specified and experimentally obtained microfiber patterns. The position errors of microfiber groups 1 and 2 are independent of the user-specified orientation, whereas the orientation errors of microfiber groups 1 and 2 appear to be inversely related to each other.

We also determine how many ultrasound transducers are needed to create any pattern of microfibers with user-specified orientation and location. Therefore, we simulate the orientation error as a function of user-specified orientation between  $0^\circ$  and  $90^\circ$  in  $1^\circ$  increments and as a function of the number of ultrasound transducers between 5 and 20 in single ultrasound transducer increments, surrounding a regular polygon-shaped reservoir with a fixed radius of 1.2 cm. Figure 6(a) shows a polygon-shaped reservoir lined with  $N_t$  ultrasound transducers (1 MHz), and with a user-specified orientation  $\theta_{\text{des}}$  that spans 1 mm (red dots) at its center. The inset shows the simulated orientation  $\theta_j$  of microfibers (black lines) based on the orientation of the local minima of the ultrasound radiation potential (see Sec. II) at each red dot along the user-specified orientation. The simulated orientation error  $\theta_{\text{sim}}$  is the absolute value of the difference between the user-specified orientation  $\theta_{\text{des}}$  and the average of all 100  $\theta_j$  values. Figure 6(b) shows the simulated orientation error as a function of the user-specified orientation and as a function of the number of ultrasound transducers  $N_t$ . From

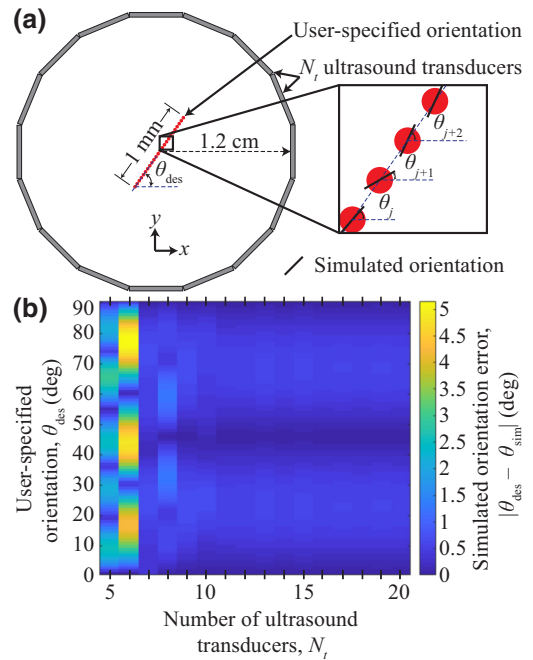


FIG. 6. (a) Polygon-shaped reservoir lined with  $N_t$  ultrasound transducers showing the user-specified orientation at the reservoir center and (b) simulated orientation error as a function of user-specified orientation and the number of ultrasound transducers.

Fig. 6(b), we observe that the effect of the user-specified orientation on the simulated orientation error is negligible for a sufficiently large number of ultrasound transducers. For a small number of ultrasound transducers (e.g.,  $N_t = 5$  and  $N_t = 6$ ), the simulated orientation error is cyclic, but trends toward zero when the user-specified orientation is parallel to any ultrasound transducer surface. For  $N_t = 5$  and  $N_t = 6$ , we observe that the orientation error trends toward zero when  $\theta_{\text{des}} = m[180(N_t - 2)/N_t - 90]^\circ$  where  $m \in \mathbb{Z}$ . This result demonstrates that in a polygon-shaped reservoir, the interference of ultrasound wave fields generated by sets of “nearly” parallel ultrasound transducers on opposing sides of the reservoir can act as a set of parallel ultrasound transducers oriented at an angle that is not physically represented by any ultrasound transducer in the system. Furthermore, this implies that with increasing  $N_t$ , the number of sets of “nearly” parallel ultrasound transducers also increases, thus reducing the orientation error for any user-specified orientation. However, a general relationship between user-specified location, user-specified angle, reservoir geometry, number of ultrasound transducers, and transducer operating parameters is complex and remains an open problem.

We point out that it is possible to specify a pattern and orientation that will not yield acoustic traps at user-specified locations or in the user-specified orientation because not all possible user-specified positions and

orientations yield a solution of Eq. (10) that also satisfies the Helmholtz equation. Furthermore, we perform experiments at one fixed frequency for practical purposes. Indeed, piezoelectric transducers typically operate close to their center frequency to obtain high-amplitude vibrations. Thus, performing the experiments at a different frequency would require using different piezoelectric transducers.

Prior to this work, the inverse ultrasound DSA problem has been solved by minimizing the acoustic radiation potential or acoustic pressure to generate acoustic traps(s) at user-specified locations to enable manipulating a single particle to follow a user-specified path [17], and to form user-specified patterns of particles [16,34–38], including experimental demonstrations of line patterns [16,20]. However, the line patterns could only be formed parallel to the ultrasound transducer surfaces. In contrast, the theoretical method and corresponding experiments in this work demonstrate the ability to form line patterns with explicitly defined user-specified orientations that are not parallel to the ultrasound transducer surfaces, thus enabling using ultrasound DSA as a manufacturing process for, for example, engineered materials that comprise aligned microfiber inclusions, such as polymer (nano)composite materials. A reservoir with a fixed arrangement of ultrasound transducers then enables aligning microfibers along any user-specified angle without having to modify the transducer arrangement. The results shown in this work demonstrate the capabilities of the ultrasound DSA alignment technique, but the range of alignment is limited by the reservoir geometry and size. Achieving long-range alignment may require a different reservoir geometry, for example, a flat array of ultrasound transducers.

#### IV. CONCLUSION

We derive a solution to the inverse ultrasound DSA problem to organize patterns of high-aspect-ratio particles with explicitly defined user-specified orientation in 2D. We demonstrate that a bead-chain model consisting of spheres enables accurately placing and orienting high-aspect-ratio particles in an ultrasound field, where for a single group of aligned microfibers, orientation and position errors remain below 12.3% and 4.6%, respectively. For multiple groups of aligned microfibers with different user-specified orientation, orientation and position errors remain below 25.2% and 13.8%, respectively. For a single group of microfibers in a reservoir consisting of 16 ultrasound transducers arranged in a hexadecagon, we can accurately orient high-aspect-ratio particles between  $0^\circ$  and  $90^\circ$  in 2D, and in orientations that are not parallel to ultrasound transducer surfaces. Similarly, we can simultaneously orient multiple groups of microfibers that do not share the same user-specified orientation. Thus, this method provides an approach to assemble user-specified

patterns of high-aspect-ratio particles with user-specified orientations.

#### ACKNOWLEDGMENTS

This research was supported by the Army Research Office under Grant No. W911NF-16-1-0457. The authors thank Dr. Asier Marzo for fruitful discussions and for providing the FPGA boards.

#### APPENDIX

Derivation of Eq. (8).

We compute the curvature  $\kappa_l$  of the acoustic radiation potential  $U_l$  in terms of the Hessian of  $U_l$  in the direction  $\hat{\mathbf{u}} = [u_x, u_y]^H$  as

$$\begin{aligned} \kappa_l &= [u_x, u_y] \begin{bmatrix} \frac{\partial^2 U_l}{\partial x^2} & \frac{\partial^2 U_l}{\partial x \partial y} \\ \frac{\partial^2 U_l}{\partial x \partial y} & \frac{\partial^2 U_l}{\partial y^2} \end{bmatrix} \begin{bmatrix} u_x \\ u_y \end{bmatrix} \\ &= u_x^2 \frac{\partial^2 U_l}{\partial x^2} + 2u_x u_y \frac{\partial^2 U_l}{\partial x \partial y} + u_y^2 \frac{\partial^2 U_l}{\partial y^2}. \end{aligned} \quad (\text{A1})$$

Here,  $\hat{\mathbf{u}}$  is of unit length. We use the definition of acoustic radiation potential in quadratic form, first presented in Ref. [16], computed as

$$U_l = \mathbf{v}^H \mathbf{Q}_l \mathbf{v}, \quad (\text{A2})$$

whose second spatial derivatives are calculated as

$$\frac{\partial^2 U_l}{\prod_{n \in x,y} \partial n} = \mathbf{v}^H \frac{\partial^2 \mathbf{Q}_l}{\prod_{n \in x,y} \partial n} \mathbf{v}. \quad (\text{A3})$$

By substituting Eq. (3) into Eq. (1), we obtain

$$\kappa_l = \mathbf{v}^H \left( u_x^2 \frac{\partial^2 \mathbf{Q}_l}{\partial x^2} + 2u_x u_y \frac{\partial^2 \mathbf{Q}_l}{\partial x \partial y} + u_y^2 \frac{\partial^2 \mathbf{Q}_l}{\partial y^2} \right) \mathbf{v}. \quad (\text{A4})$$

To compute the curvature in the direction perpendicular to a specified orientation  $\theta_l$ , we set the terms  $u_x = -\sin(\theta_l)$  and  $u_y = \cos(\theta_l)$ . Thus, we compute the curvature perpendicular to an orientation  $\theta_l$  as

$$\begin{aligned} \kappa_l &= \mathbf{v}^H \left( \sin^2(\theta_l) \frac{\partial^2 \mathbf{Q}_l}{\partial x^2} - 2 \sin(\theta_l) \cos(\theta_l) \frac{\partial^2 \mathbf{Q}_l}{\partial x \partial y} \right. \\ &\quad \left. + \cos^2(\theta_l) \frac{\partial^2 \mathbf{Q}_l}{\partial y^2} \right) \mathbf{v}. \end{aligned} \quad (\text{A5})$$

For clarity, we set

$$\begin{aligned} \hat{\mathbf{Q}}_l &= \sin^2(\theta_l) \frac{\partial^2 \mathbf{Q}_l}{\partial x^2} - 2 \sin(\theta_l) \cos(\theta_l) \frac{\partial^2 \mathbf{Q}_l}{\partial x \partial y} \\ &\quad + \cos^2(\theta_l) \frac{\partial^2 \mathbf{Q}_l}{\partial y^2}, \end{aligned} \quad (\text{A6})$$



- [1] M. Grzelczak, J. Vermant, E. M. Furst, and L. M. Liz-Marzán, Directed self-assembly of nanoparticles, *ACS Nano* **4**, 3591 (2010).
- [2] M. Evander and J. Nilsson, Acoustofluidics 20: Applications in acoustic trapping, *Lab Chip* **12**, 4667 (2012).
- [3] Y. Yamakoshi, Y. Koitabashi, N. Nakajima, and T. Miwa, Yeast cell trapping in ultrasonic wave field using ultrasonic contrast agent, *Jpn. J. Appl. Phys.* **45**, 4712 (2006).
- [4] J. N. Coleman, U. Khan, W. J. Blau, and Y. K. Gun'ko, Small but strong: A review of the mechanical properties of carbon nanotube-polymer composites, *Carbon* **44**, 1624 (2006).
- [5] V. M. Shalaev, Optical negative-index metamaterials, *Nat. Photonics* **1**, 41 (2007).
- [6] S. J. Corbitt, M. Francoeur, and B. Raeymaekers, Implementation of optical dielectric metamaterials: A review, *J. Quant. Spectrosc. Radiat. Transfer* **158**, 3 (2015).
- [7] M. D. Haslam and B. Raeymaekers, Aligning carbon nanotubes using bulk acoustic waves to reinforce polymer composites, *Composites, Part B* **60**, 91 (2014).
- [8] J. Greenhall and B. Raeymaekers, 3D printing macroscale engineered materials using ultrasound directed self-assembly and stereolithography, *Adv. Mater. Technol.* **2**, 170122 (2017).
- [9] Z. Nie, A. Petukhova, and E. Kumacheva, Properties and emerging applications of self-assembled structures made from inorganic nanoparticles, *Nat. Nanotechnol.* **5**, 15 (2010).
- [10] S. B. Darling, Directing the self-assembly of block copolymers, *Prog. Polym. Sci.* **32**, 1152 (2007).
- [11] Y. Chen, H. Liu, T. Ye, J. Kim, and C. Mao, DNA-directed assembly of single-wall carbon nanotubes, *J. Am. Chem. Soc.* **129**, 8696 (2007).
- [12] K. D. Hermanson, S. O. Lumsdon, J. P. Williams, E. W. Kaler, and O. D. Velev, Dielectrophoretic assembly of electrically functional microwires from nanoparticle suspensions, *Science* **294**, 1082 (2001).
- [13] J. H. E. Promislow and A. P. Gast, Magnetorheological fluid structure in a pulsed magnetic field, *Langmuir* **12**, 4095 (1996).
- [14] B. Raeymaekers, C. Pantea, and D. N. Sinha, Manipulation of diamond nanoparticles using bulk acoustic waves, *J. Appl. Phys.* **109**, 014317 (2011).
- [15] M. Prisbrey and B. Raeymaekers, Ultrasound Noncontact Particle Manipulation of Three-Dimensional Dynamic User-Specified Patterns of Particles in Air, *Phys. Rev. Appl.* **10**, 034066 (2018).
- [16] J. Greenhall, F. Guevara Vasquez, and B. Raeymaekers, Ultrasound directed self-assembly of user-specified patterns of nanoparticles dispersed in a fluid medium, *Appl. Phys. Lett.* **108**, 103103 (2016).
- [17] J. Greenhall, F. Guevara Vasquez, and B. Raeymaekers, Dynamic behavior of microscale particles controlled by standing bulk acoustic waves, *Appl. Phys. Lett.* **105**, 144105 (2014).
- [18] A. Marzo, S. A. Seah, B. W. Drinkwater, D. R. Sahoo, B. Long, and S. Subramanian, Holographic acoustic elements for manipulation of levitated objects, *Nat. Commun.* **6**, ncomms9661 (2015).
- [19] J. Greenhall, F. Guevara Vasquez, and B. Raeymaekers, Continuous and unconstrained manipulation of microparticles using phase-control of bulk acoustic waves, *Appl. Phys. Lett.* **103**, 074103 (2013).
- [20] M. Prisbrey, J. Greenhall, F. Guevara Vasquez, and B. Raeymaekers, Ultrasound directed self-assembly of three-dimensional user-specified patterns of particles in a fluid medium, *J. Appl. Phys.* **121**, 014302 (2017).
- [21] D. Baresch, J.-L. Thomas, and R. Marchiano, Observation of a Single-Beam Gradient Force Acoustical Trap for Elastic Particles: Acoustical Tweezers, *Phys. Rev. Lett.* **116**, 024301 (2016).
- [22] D. Baresch, J.-L. Thomas, and R. Marchiano, Orbital Angular Momentum Transfer to Stably Trapped Elastic Particles in Acoustical Vortex Beams, *Phys. Rev. Lett.* **121**, 074301 (2018).
- [23] L. P. Gor'kov, On the Forces Acting on a Small Particle in an Acoustical Field in an Ideal Fluid, *Soviet Physics Doklady* **6**, 773 (1962).
- [24] R. R. Collino, T. R. Ray, R. C. Fleming, C. H. Sasaki, H. Haj-Hariri, and M. R. Begley, Acoustic field controlled patterning and assembly of anisotropic particles, *Extreme Mech. Lett.* **5**, 37 (2015).
- [25] L. E. Kinsler, A. R. Frey, A. B. Coppens, and J. V. Sanders, *Fundamentals of Acoustics*, 4th ed. (John Wiley, New York, 2000).
- [26] C. R. P. Courtney, B. W. Drinkwater, C. E. M. Demore, S. Cochran, A. Grinenko, and P. D. Wilcox, Dexterous manipulation of microparticles using Bessel-function acoustic pressure fields, *Appl. Phys. Lett.* **102**, 123508 (2013).
- [27] Y. Ochiai, T. Hoshi, and J. Rekimoto, Three-dimensional mid-air acoustic manipulation by ultrasonic phased arrays, *PLOS ONE* **9**, e97590 (2014).
- [28] A. Marzo, A. Barnes, and B. W. Drinkwater, TinyLev: A multi-emitter single-axis acoustic levitator, *Rev. Sci. Instrum.* **88**, 085105 (2017).
- [29] D. Foresti, M. Nabavi, M. Klingauf, A. Ferrari, and D. Poulikakos, Acoustophoretic contactless transport and handling of matter in air, *Proc. Natl. Acad. Sci. U.S.A.* **110**, 12549 (2013).
- [30] M. Barmatz and P. Collas, Acoustic radiation potential on a sphere in plane, cylindrical, and spherical standing wave fields, *J. Acoust. Soc. Am.* **77**, 928 (1985).
- [31] X. Chen and R. E. Apfel, Radiation force on a spherical object in an axisymmetric wave field and its application to the calibration of high-frequency transducers, *J. Acoust. Soc. Am.* **99**, 713 (1996).
- [32] D. Baresch, J.-L. Thomas, and R. Marchiano, Three-dimensional acoustic radiation force on an arbitrarily located elastic sphere, *J. Acoust. Soc. Am.* **133**, 25 (2013).
- [33] D. Baresch, J.-L. Thomas, and R. Marchiano, Spherical vortex beams of high radial degree for enhanced single-beam tweezers, *J. Appl. Phys.* **113**, 184901 (2013).
- [34] C. R. P. Courtney, C.-K. Ong, B. W. Drinkwater, A. L. Bernassau, P. D. Wilcox, and D. R. S. Cumming, Manipulation of particles in two dimensions using phase controllable ultrasonic standing waves, *Proc. R. Soc. A* **468**, rspa20110269 (2011).

- [35] C. R. P. Courtney, C. E. M. Demore, H. Wu, A. Grinenko, P. D. Wilcox, S. Cochran, and B. W. Drinkwater, Independent trapping and manipulation of microparticles using dexterous acoustic tweezers, *Appl. Phys. Lett.* **104**, 154103 (2014).
- [36] A. L. Bernassau, C. R. P. Courtney, J. Beeley, B. W. Drinkwater, and D. R. S. Cumming, Interactive manipulation of microparticles in an octagonal sonotweezer, *Appl. Phys. Lett.* **102**, 164101 (2013).
- [37] Bernassau, A. & Cumming, D. R. S. Acoustic Tweezing at the Nodes or Antinodes of a Heptagonal Multi Piezoelectric Transducer Cell, 1537 (2011).
- [38] A. Grinenko, P. D. Wilcox, C. R. P. Courtney, and B. W. Drinkwater, Proof of principle study of ultrasonic particle manipulation by a circular array device, *Proc. R. Soc. A* **468**, 3571 (2012).
- [39] T. Schwarz, G. Petit-Pierre, and J. Dual, Rotation of non-spherical micro-particles by amplitude modulation of superimposed orthogonal ultrasonic modes, *J. Acoust. Soc. Am.* **133**, 1260 (2013).
- [40] M. Scholz, B. W. Drinkwater, T. M. Llewellyn-Jones, and R. S. Trask, Counterpropagating wave acoustic particle manipulation device for the effective manufacture of composite materials, *IEEE Trans. Ultrason. Ferroelectr. Freq. Control* **62**, 1845 (2015).
- [41] L. C. Wrobel and M. H. Aliabadi, *The Boundary Element Method, Applications in Thermo-Fluids and Acoustics* (Wiley, Hoboken, NJ, 2002).